Regular Paper

Assessment of geomembrane strain from pond liner bubbles

H.M.G. Eldesouky [a], R. Thiel [b], R.W.I. Brachman [c,*]

[a] *WSP E&I Canada Ltd, Vancouver, BC, V6B 5W3, Canada*
[b] *Thiel Engineering, Oregon House, CA, 95962, USA*
[c] *GeoEngineering Centre at Queen's–RMC, Queen's University, Kingston, ON, K7L 4P5, Canada*

ARTICLE INFO

ABSTRACT

Bubbles (a.k.a. whales) that develop from gas entrapped beneath a geomembrane in pond liner applications lead to localized increases in geomembrane strain that warrant evaluation. Results from three-dimensional, geometrically-nonlinear, finite-element analysis are presented to show how geomembrane stiffness, fluid depth, volume of entrapped gas, and interface friction affect the deformed shape of, and maximum strain in the geomembrane. It is shown that the deformed geomembrane follows a bell-shaped curve and that geomembrane strain increases as the fluid depth increases until the bubble is submerged. The extent to which the maximum strain increases with decreasing geomembrane stiffness and increasing volume of entrapped gas are quantified. Design and operation charts are presented to provide a practical means of assessing strain in existing geomembrane bubbles or identify maximum fluid depths to limit geomembrane strain to a target value.

1. Introduction

Obtaining a relative level of impermeability is key when selecting a liner for fluid containment in environmentally sensitive applications like process ponds for mining, leachate ponds for municipal and hazardous waste landfills, and industrial and municipal wastewater treatment ponds (e.g., Lavoie et al., 2022; 2021; 2020; Nower et al., 2020; Sharma et al., 2023). Intact geomembranes provide flexible fluid barriers, which, since the 1940's, have been used as pond liners instead of other options (e.g., concrete, asphalt and low-permeability soils). Often for cost and maintenance reasons, many geomembrane-lined ponds are designed and constructed with an exposed single geomembrane, without any soil covering or ballast. One of the design and operational challenges with this configuration is that gas can accumulate beneath the geomembrane and create a localized zone that is lifted off the underlying surface (Fig. 1), herein denoted as a bubble. They have also been referred to colloquially using the zoomorphism, whales or hippos (Gassner, 2017; Guo et al., 2016; Marta and Armstrong, 2020).

The gas may be from: entrapped air beneath geomembrane wrinkles formed during installation (Gassner, 2017; Thiel, 2016a; 2016b; Wallace et al., 2006), emissions generated by biologically active wastewater that leaked beneath the geomembrane (Koerner, 2005; Thiel and Giroud, 2011), or expulsion of air from the subgrade due to a rise in the groundwater table (Giroud and Goldstein, 1982; Guo et al., 2016; Wang

et al., 2020). Several complications may arise from bubbles, including: a) the loss of pond storage volume, b) increased leakage from the pond by creating a geomembrane region with no subgrade contact, c) boats or other equipment can cause mechanical damage to the geomembrane, d) poor aesthetics for decorative ponds, e) extreme stretching, or bursting, of the geomembrane due to the strains imposed by the gas pressure, and f) potential damage to the geomembrane as the exposed parts of bubble are subjected to cyclic stress due to wind, waves, and thermal cycles (Marta and Armstrong, 2020; Peggs, 2012).

Methods have been proposed to model geomembrane bubbles. For example, Guo et al. (2016) modelled the geomembrane as a thin shell with uniform tensile force subject to internal bubble pressure and external fluids pressure to solve for bubble geometry and geomembrane tensile force. Thiel (2016a) assumed the general form of the deformed bubble shape (circular on top down to a point of inflection and then as a clothoidal spiral until reaching a point of tangency with the subgrade) and considered force equilibrium to iteratively solve for bubble height, diameter, pressure and geomembrane strain. Both methods neglected interface friction between the geomembrane and the subgrade. In terms of geomembrane strain, the first method had no explicit mention of the distribution or magnitude of geomembrane tensile strain, whereas the second assumed constant strain across the top of the bubble and concentrated strain near its edge. While geomembrane strain has been investigated for bottom liner applications (e.g., Eldesouky and

Brachman, 2018; 2023; Marcotte and Fleming, 2021; 2022; Fan and Rowe, 2022) there is a paucity of data on strain developed from geomembrane bubbles.

Three-dimensional, geometrically-nonlinear, finite-element analysis is an alternate approach to model bubble formation and geomembrane strains. By simultaneously solving force-equilibrium and strain-displacement equations as the geometry of the bubble changes from increases in fluid depth, the finite-element analysis would be expected to capture the dominant influences on geomembrane strain (e.g., vertical and radial displacements) without the previous simplified idealizations, other than the form of a constitutive model between stress and strain. Such finite-element analysis with a linear, elastic constitutive model was used by Thiel et al. (2022) to compare with the two existing methods for one particular set of parameters. For a fluid depth of 2 m, bubble height of 3.6 m and geomembrane stiffness of 300 kN/m, the bubble radius and strain at the water line from Thiel's (2016a) method were within 7.4% and 13%, respectively, of the values calculated from the finite-element analysis, while bubble radius from Guo et al. (2016) was within 3.2% of that from the finite-element analysis. While the results from the two simplified methods were found to be relatively close to those from the finite-element analysis, additional evaluation of geomembrane strain is warranted given the importance of limiting strain to prevent geomembrane rupture.

The objective of this paper is to quantify the geomembrane strain from pond liner bubbles using three-dimensional, geometrically-nonlinear, finite-element analysis. The effects of geomembrane stiffness, fluid depth, volume of entrapped gas, and interface friction on the deformed bubble shape and hence the pattern and magnitude of geomembrane strain are examined. Parametric studies of geomembrane strain, bubble size, bubble pressure and submergence depth are presented for a wide range of practical cases. Design and operation charts are presented to provide a practical means of assessing strain in existing geomembrane bubbles or identify maximum fluid depths to limit geomembrane strain to a target value.

2. Bubble formation and factors affecting bubble size

In a field case study, Wallace et al. (2006) reported formation of bubbles in a pond from entrapped air beneath geomembrane wrinkles. Pockets of air can accumulate under the geomembrane during installation. As the pond is being filled, the water begins to coalesce wrinkles into floating air pockets. If the pond bottom is not sufficiently sloped to allow the air pockets to be driven upslope, or if the pond does not have an unsaturated gas venting system below the geomembrane to allow the air pressure to freely vent, then the loose air pockets will progressively accumulate into discrete bubbles. Theses bubbles would accumulate under localized high points in the liner subgrade. The initial volume of entrapped air and the ability of the air to accumulate into bubbles are the two main factors affecting the bubble size, which in turn affects the bubble pressure and geomembrane strains.

For purposes of providing a context for examining the factors affecting bubble formation, size and strain, the modelling in this paper considers bubbles accumulating over a circular pond region with radius R (Fig. 1) that is lined with a single geomembrane. The results can also be used for square ponds with width S. The initial entrapped air is taken to be randomly distributed beneath the wrinkles existing in the newly installed geomembrane and the total volume of entrapped air depends on the cumulative size of the wrinkles. In the worst case, all the air entrapped would accumulate in one single large bubble during pond filling. Engineered features (e.g., partition ballast, intermediate anchor trenches, unsaturated transmissive venting strips) can be designed to isolate the entire pond into different zones that would contain the entrapped air and hence any resulting bubbles within each zone. This in turn would reduce the maximum volume of a bubble in subdivided regions of the pond and the entrapped air would accumulate into several smaller bubbles rather than larger ones. As such, and for a square region of pond with dimension S, the values of S considered in Table 1 could represent as large as a 100 × 100 m pond to a much smaller 10 × 10 m pond without any partitioning measures, or an even larger pond if it were subdivided into smaller partitioned zones with dimensions $S \times S$.

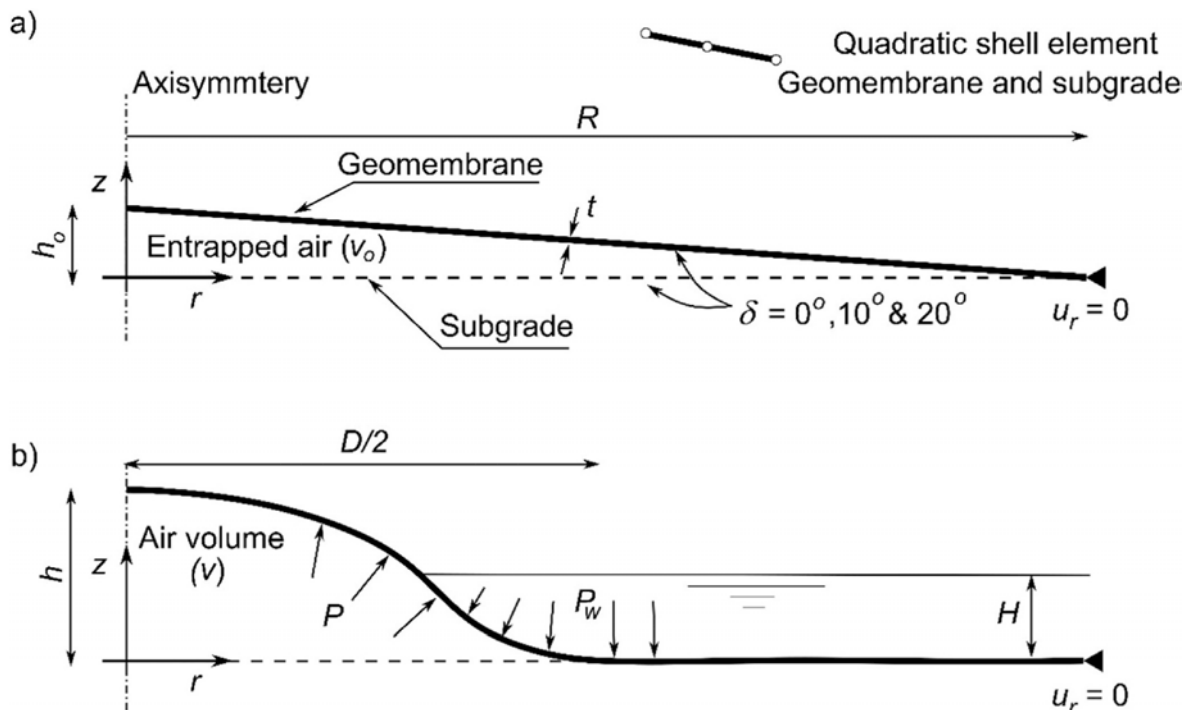There is a paucity of data on the volume of entrapped air beneath

Fig. 1. Problem definition. a) Geomembrane with initial volume of entrapped air *vo*. b) Development of geomembrane bubble under external fluid pressure P_w and internal air pressure P.

Table 1
Initial bubble volume v_o [m³] for pond region $S \times S$ and entrapped air volume per unit area.

S [m]	Entrapped air [cm³/m²]			
	65,000	52,500	39,000	26,000
100	650	525	390	260
50	163	131	98	65
20	26	21	16	10
10	7	5	4	3

geomembrane wrinkles. Wallace et al. (2006) made estimates of the frequency and size of wrinkles in a newly installed pond and estimated the entrapped air volume to be between 50 and 100 m³ beneath a 105 m × 178 m pond, which would correspond to an entrapped air volume per unit area between 2700 and 5500 cm³/m². In the case of a 100 × 100 m (1 ha) pond, this range would represent a total entrapped air volume from 27 to 55 m³. Wallace et al. (2006) estimated that the average bubble size experienced in their case history was on the order of 3 m³, which tends to the smaller range of bubble size that have been observed at other sites. Towards the upper end, Thiel (2016a) reported on a single bubble with a diameter greater than 35 m, height greater than 8 m, and total volume approaching 4000 m³, while Gassner (2017) also reported a bubble size with an estimated diameter of 35 m. While these large bubbles were formed in significantly larger (>30 ha) ponds, corresponding to ρ up to 13,000 cm³/m², these case histories serve to demonstrate the range of potential bubble sizes that were considered in the analysis. In field studies, wrinkles were found to cover up to 32% of the liner area with a height up to 15 cm (Chappel et al., 2012; Rentz et al., 2017; Rowe et al., 2012). The entrapped air volume can be estimated by approximating the wrinkle section as an isosceles triangle, and therefore, the volume of air entrapped under a single wrinkle would be 0.5 x wrinkle height x wrinkle width resulting in ρ up to 24,000 cm³/m². However, wrinkles with a height less than 3 cm were not considered in these studies which would underestimate the volume of entrapped air. The values of ρ between 26,000 and 65,000 cm³/m² considered in this work lead to initial volumes of entrapped gas between 3 and 650 m³ for the range of R values given in Table 1. The simulation resulted in bubbles with diameters as large as those reported by Thiel (2016a) and Gassner (2017).

3. Finite-element analysis

Three-dimensional, geometrically-nonlinear, finite-element analysis was conducted with the commercially available program ABAQUS (2017). The axisymmetric geometry and solution domain with polar coordinates r and z are shown in Fig. 1. The geomembrane, with thickness t, was modelled by 200 equally-spaced, quadratic shell-elements, which was shown to be numerically sufficient by progressively increasing the number of elements until the maximum calculated strain changed by no more than 0.5%. A zero radial and vertical displacement boundary was modelled around the perimeter of the geomembrane ($u_r = u_z = 0$ at $r = R$; Fig. 1) while zero radial displacement and zero angular rotation were imposed at its centre ($u_r = 0$ and $r = 0$). The initial air volume v_o was assumed to occupy a conical shaped zone beneath the otherwise initially flat geomembrane (Fig. 1a).

The geometry of the mesh was then updated (i.e., geometrically nonlinear analysis) as the fluid pressure increased, pressing the geomembrane down until new contact with the subgrade was formed, as well as radially compressing the bubble, along with increasing height from the internal air pressure. External fluid pressures were modelled as hydrostatic (with unit weight of 9.8 kN/m³). Internal gas pressures were calculated as proportional to volume change of the airspace encapsulated by the bubble using the ideal gas law:

$$P_a v_o = (P + P_a) v \qquad [1]$$

where: P_a is atmospheric pressure, v_o is the initial volume of entrapped gas, and P is the new gauge pressure for deformed volume v. This approach assumes that no gas escapes into the underlying soil and as such may overestimate internal pressure effects for gas permeable unsaturated subgrades. The interface between the geomembrane and the underlying rigid subgrade was modelled as frictional with angle of interface friction, δ, equal to 0, 10 or 20°. Fluid depth was increased in steps no greater than 0.1 m. For each step, the deformed shape, internal and external pressure, and contact with the subgrade were iterated until equilibrated with internal geomembrane forces to convergence tolerance less than 0.5%.

As a first approach, and as consistent with the more approximate methods of Guo et al. (2016) and Thiel (2016a), the geomembrane was modelled with stress linearly proportional to strain with elastic modulus E and Poisson's ratio (taken equal to 0.46) and independent of temperature. For time and temperature dependent materials, the rate at which the bubble develops and the duration that the bubble is sustained may be important and with a linear elastic model at best can be accounted for by appropriate selection of secant values of modulus at a given temperature. Although beyond the scope of this paper, additional work on time and temperature effects may be warranted.

While selection of geomembrane stiffness ($E \times t$, simply denoted herein as Et) should be selected based on the materials and conditions for any particular project, results are presented over a wide range of stiffnesses (150–1500 kN/m) intended to bracket most practical applications. For context only, typical low-strain (<4%) E values reported for common geomembrane materials measured in uniaxial tests at standard laboratory temperature reported by Koerner (2005) are 330, 76, 25, and 330 MPa for HDPE, VLDPE, PVC, and reinforced CSPE, respectively. Giroud et al. (1993) indicated uniaxial secant E values for HDPE at 4% strain of 460, 340, and 300 MPa at temperatures of 0, 20, and 40 °C, respectively, which would be applicable to many pond applications both below and above the water. Both the Koerner (2005) and Giroud et al. (1993) HDPE data were for pre-1993 materials when slightly higher density HDPE geomembrane resins were being used. Based on more recent data reported for an HDPE geomembrane by Eldesouky and Brachman (2020) – see their work for the index properties and strain rates examined – a longer term modulus tended from 250 to 200 MPa at 4% elongation (at 20°). Additional recent data (e.g., Rarison et al., 2022; Zhang et al., 2023) provides additional guidance to estimate modulus values.

Unfortunately, there is no data set of sufficient scale to independently validate the model calculations. However, this type of geometrically-nonlinear finite-element analysis has been validated against measured values from wide-strip testing and, at a much smaller scale, for local indentations caused by gravel-sized probes by Eldesouky and Brachman (2020). Additionally, as previously noted and documented by Thiel et al. (2022), the finite-element analysis was able to reproduce the bubble shape and size calculated using the Thiel (2016a) method and that are consistent with the available field observations.

4. Results and discussion

4.1. Deformed shape and strain for a large bubble

The development of a bubble in a low stiffness geomembrane with no interface friction ($Et = 150$ kN/m, $\delta = 0°$) and relatively large entrapped volume ($v_o = 650$ m³) is shown in Fig. 2. Generally, the bubble had a Gaussian bell shape with the apex at $r = 0$, and the bubble height, h, remained above the fluid depth, H, during pond filling. The shape then sloped downward, reaching a point of inflection below water surface, reversing curvature until it reached the subgrade at the bottom edge of submerged bubble at $r=D/2$, where D is the bubble diameter (Fig. 1b). Initially, the geomembrane was relatively flat and as the water height increased from 0 to 1 m the bubble started to form, with a diameter of 20.9 m and a height of 4.1 m, Fig. 2a. With further increases in water
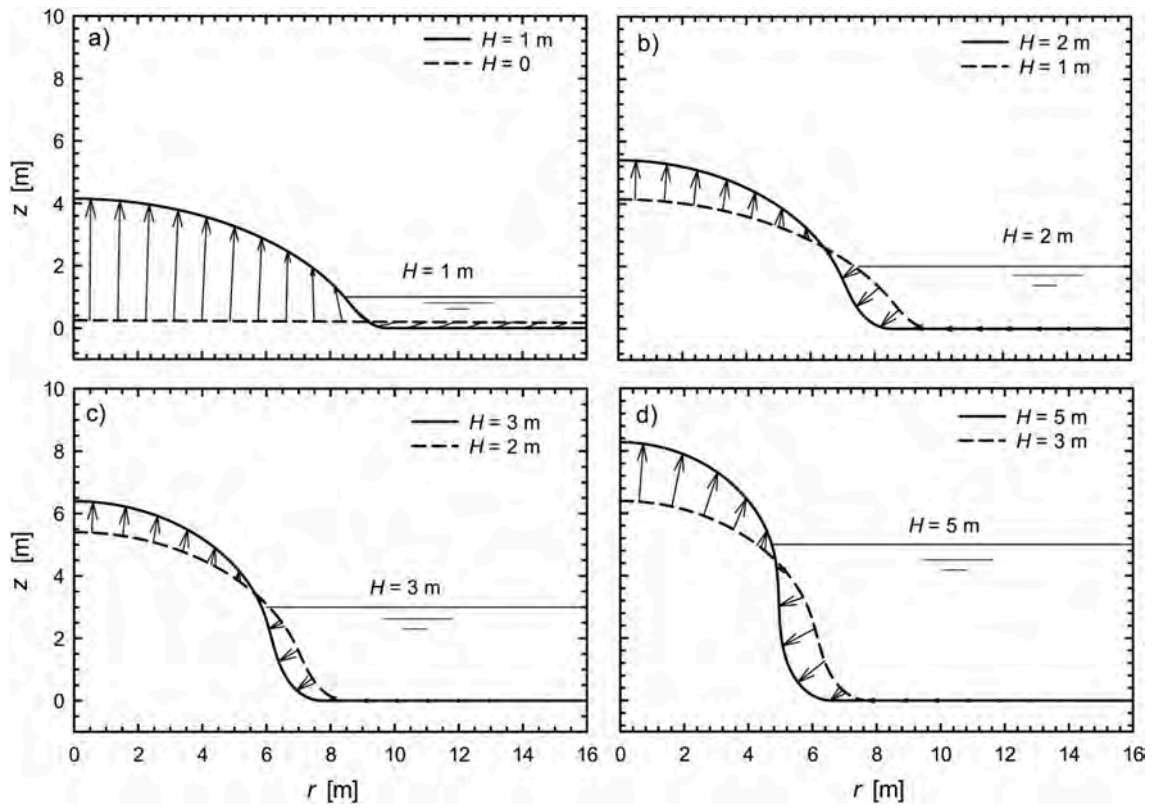
Fig. 2. Development of bubble deformed shape for a relatively flexible geomembrane. ($Et = 150$ kN/m^3, $\delta = 0$, $v_o = 650$ m^3, S = 100 m).
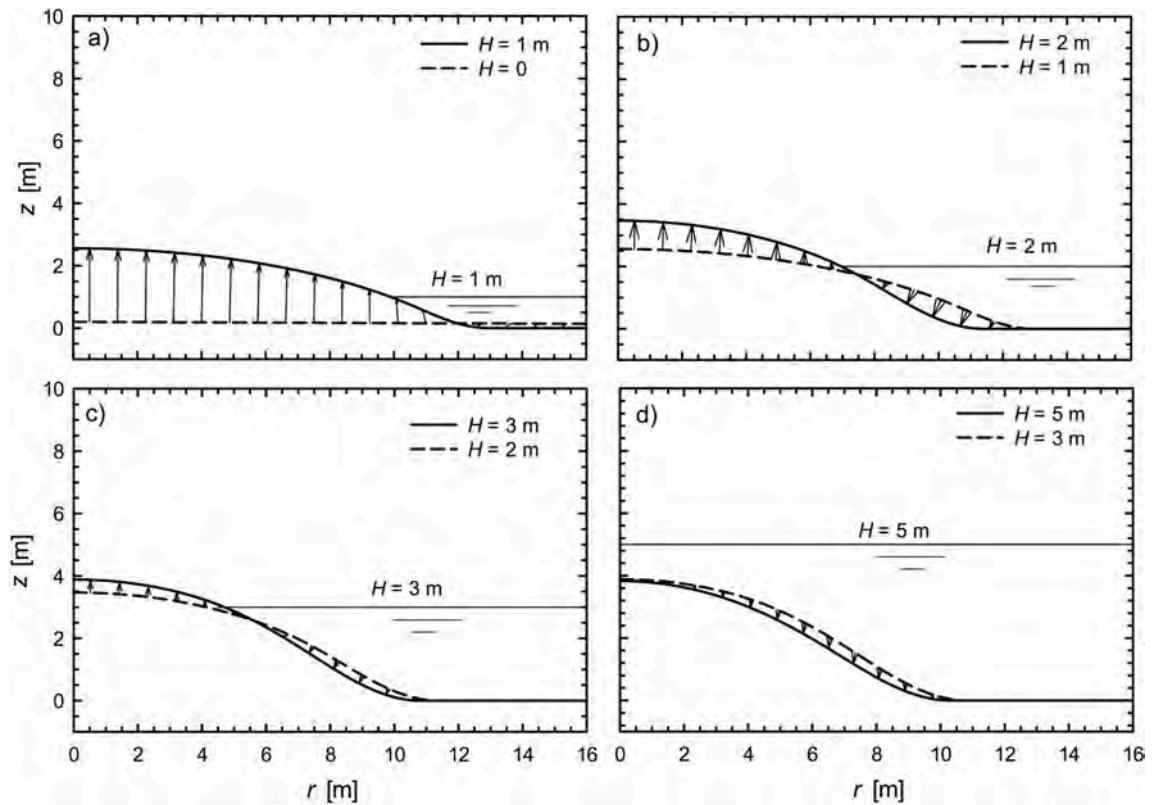

Fig. 3. Development of bubble deformed shape for a relatively stiff geomembrane. ($Et = 1500$ kN/m3, $\delta = 0$, $v_o = 650$ m^3, S = 100 m).

height to H=2, 3 and 5 m, the submerged geomembrane portion was radially compressed causing the bubble to decrease in diameter to $D = 19.1$, 18.2 and 16.9 m, respectively, and the central portion was displaced upward and outward increasing the bubble height to $h = 6.4, 7.3$ and 8.3 m, correspondingly, Fig. 2b–d.

Large bubbles formed in a higher stiffness geomembrane ($Et = 1500$ kN/m, $\delta = 0°$, $v_o = 650$ m³; Fig. 3), for otherwise the same conditions were flatter, larger in diameter and shorter in height, than the low stiffness geomembrane. The initially flat geomembrane deformed into a bubble with diameter of 25.3 m and height of 2.6 m when the fluid depth increased to $H = 1$ m, Fig. 3a. With a similar trend to the low stiffness geomembrane, the diameter decreased to $D = 21.4$ and 22.1 m and height increased to $h = 3.5$ m and 3.9 m when the fluid depth increased to $H = 2$ and 3 m, respectively, Fig. 3b and c. However, when increased to $H = 5$ m, the fluid submerged the high stiffness geomembrane and both the diameter and height decreased to $D = 21.1$ and $h = 3.8$ m, Fig. 3d. Like the low stiffness geomembrane, the submerged portion of the high stiffness geomembrane deformed inward while the central portion deformed upward and outward, but to a lesser degree. However, the entire geomembrane deformed inward and downward once the bubble was entirely submerged.

It was assumed that there was only gas inside the bubble. Any fluid within the bubble would presumably counteract some of the radial bubble compression from external fluid pressure. Neglecting these effects may overestimate bubble height for the more flexible and deeper pond cases considered, as radial compression effects are most prominent for the case in Fig. 2d and much less so for the case in Fig. 3d.

The deformed shape not only provides the height and diameter of the bubble as fluid levels change, but it reveals how and where strain develops in the geomembrane from bubble expansion. Strain mobilized in the geomembrane depends on both the radial and vertical components of displacements. While it is evident from the displacement vectors in Figs. 2 and 3 that vertical displacements are much greater than those in

the radial direction, it is the rate of change of the radial displacements relative to radial position that dominate the resulting strains in the geomembrane (Eldesouky and Brachman, 2018). The distributions of radial displacements for the low and high stiffness cases are consequently examined in Fig. 4. Changes in radial displacement u_r along the bubble were more abrupt as the water height increased. For the low stiffness case at $H = 1$ m, radial displacement changed by 0.15 m over a distance of 2 m, while at $H = 5$ m, the rate of radial displacement change was increased 46 times as radial displacement changed by 2.8 m over a distance of 5 m (Fig. 4a). These displacement gradients are reflected in the calculated radial strain ε_r magnitude and distribution, Fig. 4b, where the maximum radial strain ε_{max} increases from just under 10% to nearly 40% as the fluid depth was increased from H=1–5 m. At most fluid depths, the maximum radial strain was calculated at the bubble perimeter and below the fluid level; however, for the largest fluid depth considered (H=5 m), the maximum radial strain was calculated at the centre ($r = 0$; Fig. 4b). Beyond the outer perimeter of the bubble, the radial displacements approach zero at r=R, and correspondingly, radial strain approaches zero.

The high stiffness geomembrane reduced the calculated radial displacement by a factor of 5. For example, the maximum radial displacement calculated during at $H = 5$ m was 0.35 m for $Et = 1500$ kN/m, compared to 2 m when $Et = 150$ kN/m, (Fig. 4c vs. 4a). Therefore, the rate of radial displacement is more gradual for the high than the low stiffness geomembrane, and hence, the strain is up to 86% smaller for the stiffer geomembrane. The maximum strain increased from 2% to just over 5% as H increased from 1 to 5 m (Fig. 4d), with the maximum occurring along the bubble perimeter.

Maximum strains for the bubbles with the greatest value of entrapped gas considered ($v_o = 650$ m³) are plotted versus fluid depth and for a range of stiffness values in Fig. 5 along with bubble dimensions. For otherwise the same conditions, both bubble height and strain depend on geomembrane stiffness. For example, bubble height increases by a factor
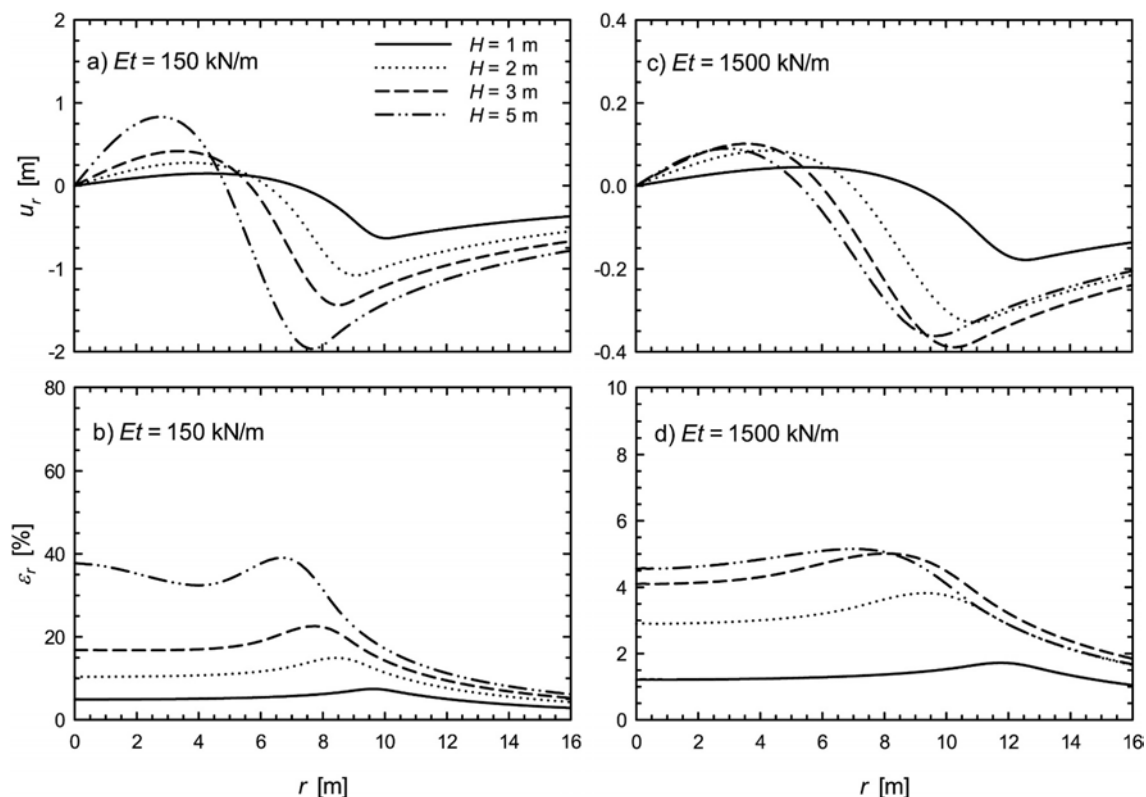

Fig. 4. Development of radial displacement (u_r) and strain (ε_r) for relatively flexible (a, b) and stiff (c, d) geomembranes as fluid depth increases. ($\delta = 0$, $v_o = 650$ m³, $S = 100$ m).
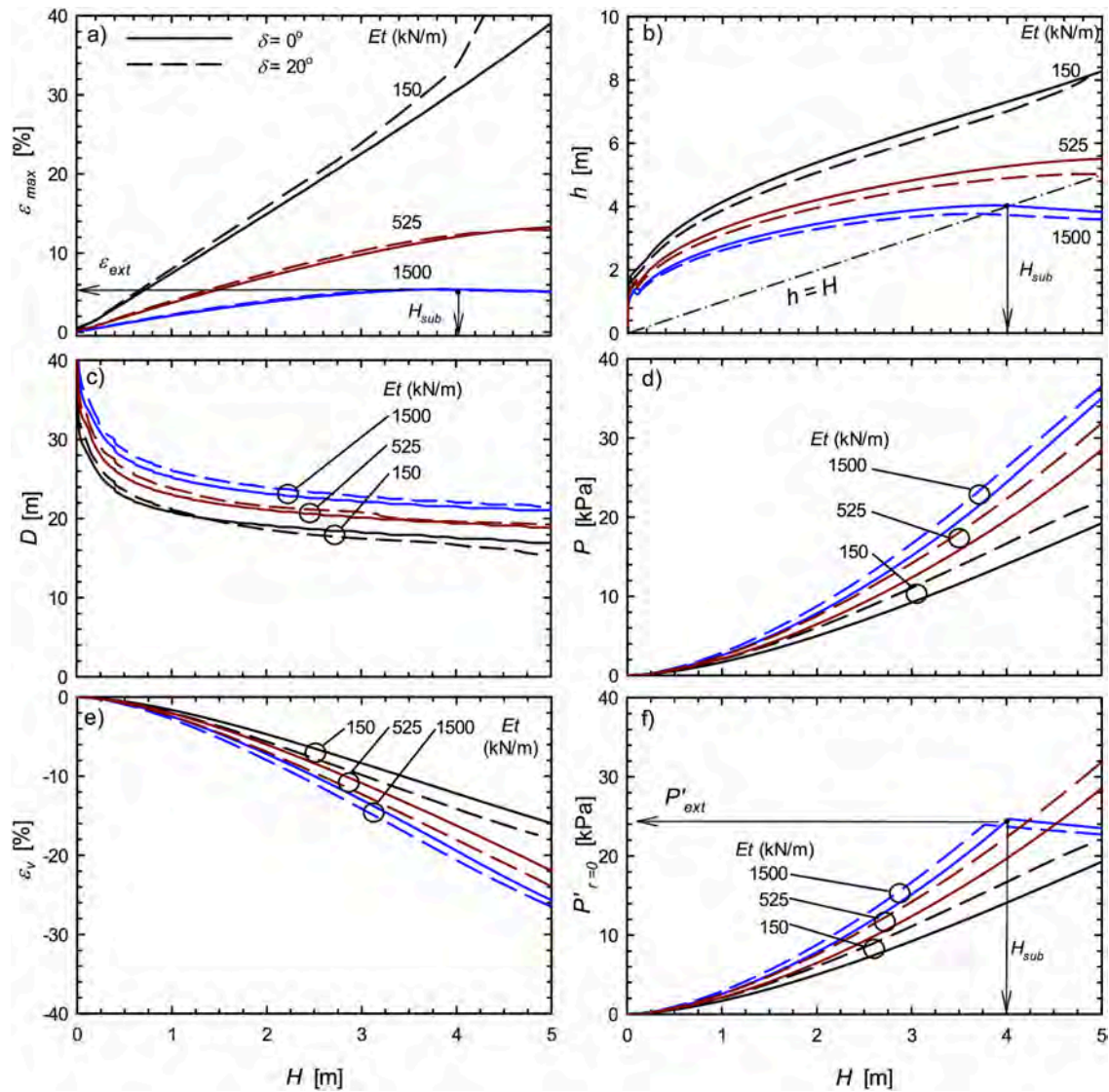
Fig. 5. Parametric study of bubble parameters to geomembrane stiffness, interface friction, and fluid depth. a) Maximum strain, b) bubble height, c) bubble diameter, d) internal pressure, e) volume strain, and f) net pressure at bubble centre. ($v_o = 650$ m^3, $S = 100$ m).

of 1.4 and strain by a factor of 4 as stiffness decreases from 1500 to 150 kN/m in a 2 m deep pond, and by greater amounts for deeper ponds (Fig. 5a and b). Strains are most sensitive to fluid depth for the lowest value of geomembrane stiffness examined ($Et = 150$ kN/m) and increase nearly linearly with H for depths up to 4 m (Fig. 5a), which up to this point, the bubbles are less than half-way submerged (Figs. 2 and 5b). For the stiffer geomembranes considered, strains also increase with H but reach a maximum value once the bubble is submerged by the fluid, where submergence is indicated by the $h = H$ line in Fig. 5b. The bubble is submerged for $H > 4$ m when $Et = 1500$ kN/m and $H \approx 5$ m for $Et = 525$ kN/m. After submergence, the bubble height then decreases and strains slightly decrease from incremental compression effects from the external fluid.

As fluid depth increases, the net effects of the increase in bubble height and decrease in bubble diameter (Fig. 5b and c) are such that gas pressure within the bubble, P, increases (Fig. 5d) and its volume decreases (expressed as a negative volumetric strain in Fig. 5e). Gas pressures increase with increasing fluid depth and increasing geomembrane stiffness. The net pressure supported by the geomembrane ($P' = P - P_w$) at $r = 0$ increases with fluid depth, and is the same as the air pressure P, until it reaches a value P'_{ext} when the bubble becomes completely submerged, Fig. 5f.

As previously noted, the results in Figs. 2–4 were obtained assuming no interface friction between the geomembrane and the subgrade ($\delta = 0$), but no significant effect was found for most practical cases when an interface friction angle of 20° was modelled, as shown in Fig. 5. An additional case of 10° was modelled but not shown in Fig. 5, as there was no discernible difference to the 20° results. Interface friction tends to decrease the inwards radial displacements of the geomembrane beside the bubble and in contact with the subgrade, which decrease the height, increase the diameter, increase the pressure, and increase the volumetric contraction. Interface friction had essentially no effect on strain for the intermediate and high stiffnesses examined (Fig. 5a). Even for the low stiffness case, there was no significant effect on strain for most practical cases. For example, for $Et = 150$ kN/m and at $H = 3$ m, the maximum strain was only 1.04 times greater with 20° interface friction relative to having none. It was only for the low stiffness geomembrane at pond depths greater than 4 m where the difference between 0 and 20° interface friction became more apparent; however, such extreme cases may be more academic than practical. Nevertheless, given that interface friction could increase strain, the design aids presented later in the paper were all obtained for an interface friction angle of 20°.
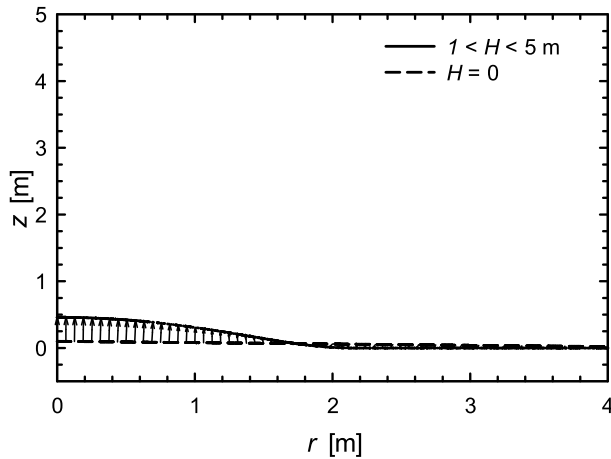
Fig. 6. Development of bubble deformed shape for a relatively flexible geomembrane and a small volume of entrapped air. ($Et = 150$ kN/m^3, $\delta = 0$, $v_o = 3$ m^3, $S = 10$ m).

4.2. Deformed shape and strain for a small bubble

The deformed shape, strain and other bubble parameters are plotted for a relatively small volume of entrapped gas ($v_o = 3$ m^3) in Figs. 6 and 7. The bubble shape still follows a Gaussian bell shape, but the maximum height does not exceed 0.5 m for all fluid depths considered (Fig. 6). Note the more than 10 fold difference in scale for strain in Fig. 7a relative to Fig. 5a. Strains still increase with decreases in geomembrane stiffness, but values do not exceed 2% for the low stiffness case, nor 0.3% for the high stiffness geomembrane (Fig. 7a). These small bubbles are completely submerged very early during the filling process, Fig. 7b, at $h = 0.47$ m for the low stiffness case and as little as $h = 0.25$ m for the high stiffness case. Bubble height and strain then decrease for fluid depths beyond submergence to the point that they would pose little risk of material failure for most typical cases. This all arises from the small initial volume of entrapped gas that generates only short, submerged bubbles, which can be obtained, in theory, by partitioning the base of a much larger pond to into $S = 10$ m regions (Table 1).

4.3. Submerging bubbles

In practice, increasing the fluid depth of the pond to submerge bubbles is one of techniques that pond operators are sometimes tempted to implement with the intention to shrink (or possibly even hide) the bubbles. The pond depth required to submerge a wrinkle, H_{sub}, and the overall maximum strain experienced by the geomembrane, herein denoted as extreme strain ε_{ext}, depend on both the volume of entrapped gas (and hence bubble height) and geomembrane stiffness as quantified in Figs. 8 and 9.

For large bubbles, $v_o = 650$ to 260 m^3, pond depths greater than 5 m would be required to submerge the bubble with a geomembrane stiffness $Et = 150$ kN/m, while depths of 5.0 to 3.8 m, 4.8 to 3.0 m and 3.9 to 2.5 m would submerge bubbles with stiffnesses of $Et = 300$, 700 and 1500 kN/m, respectively, Fig. 8. The submerging water depth significantly decreases as initial bubble size decreases. Bubbles with v_o less than 250 m^3 were completely submerged at depths less than 5 m. The submerging water height decreased by about 50–60% for every 75% decrease in initial bubble volume. Small bubbles with v_o less than 10 m^3, were submerged at depths less than 1 m, even for the lowest stiffness examined. The results in Fig. 8 were obtained modelling zero interface friction between the geomembrane and subgrade, and were no more than 10% smaller when 20° interface friction was considered.

In some of the cases considered, mainly those for large bubbles with low geomembrane stiffness, complete submergence of the bubbles was not reached up to $H = 5$ m, and for these cases, the values of the extreme strain were plotted in Fig. 9 as the values for H=5 m. More than one order of magnitude reduction in extreme strain was calculated when the geomembrane stiffness increased from $Et = 150$–1500 kN/m (Fig. 9). Approximately two thirds of the extreme strain value reduction occurred as the geomembrane stiffness increased from $Et = 150$–525 kN/m. For example, for $v_o = 390$ m^3, the extreme strain was 37, 10 and 3% for stiffnesses of 150, 525 and 1500 kN/m, respectively (Fig. 9). Smaller bubbles also showed a significant reduction in calculated extreme strain as geomembrane stiffness increased, with about 50–80% of the reduction occurring as the geomembrane stiffness increased from 150 to 525 kN/m. The calculated extreme strain was reduced by almost one-half for every 4 fold reduction in initial bubble volume.

The results in Fig. 9 were also obtained modelling zero interface friction between the geomembrane and subgrade, but there was no practical difference in extreme strain (less than 4% difference) for stiffness values greater than 400 kN/m when 20° interface friction was considered. The increase in strain with 20° interface friction increased with increasing volume and decreasing stiffness and exceeded 20% for stiffnesses less than 200 kN/m. For such cases, the design aids presented in the following section would provide better estimates of strain.

It should be noted that even if a bubble is successfully submerged without compromising the integrity of the geomembrane, there are still the corollary effects of lost pond capacity, endangerment of the geomembrane due to its physical protrusion above the pond bottom, potential for increased leakage if there are any defects in the geomembrane, and invitation for ground water or leakage to fill the bubble from below and create a more complex problem. At the same time, the presence of a visible bubble in the pond should be a warning that significant consequences of geomembrane failure could occur if some precautions are not observed, namely, controlling the water height to a level that would hopefully avoid damaging strains from occurring in the geomembrane. Therefore, assessing the geomembrane strain in a developed bubble and the expected strain, when water height is changed, are key factors in bubble management decisions.

5. Practical application

5.1. Design and assessment aids

The finite-element analysis was used to calculate and then tabulate the maximum geomembrane strain for a wide range of bubble, pond, and geomembrane parameters with the intent of providing practitioners with a straightforward means of estimating strain during design or assessing strain during operation. They are shown in Fig. 10 for one particular value of geomembrane stiffness (375 kN/m) and are available as Supplemental Material (Fig. A1) for the entire range of stiffnesses considered (150–1500 kN/m). The initial gas volume (v_o) and fluid depth (H) are the input variables for each value of geomembrane stiffness and the output is presented in one of two forms. The first (Fig. 10a, b and c), relate bubble volume to the initial volume and depth, while the second, relate maximum geomembrane strain to initial volume and depth (Fig. 10d, e, and f). Values are provided for different sizes of bubbles, with v_o ranging from 3 to 650 m^3. All charts were obtained from models with an interface friction angle of 20°.

In a design situation, strain can be obtained for an anticipated range of initial gas volumes and candidate geomembrane based on its stiffness from the plots like Fig. 10d, e, and f. In an assessment situation, where bubble diameter D and height h can be measured by surveying, the current bubble volume v can be estimated by assuming the bubble follows a Gaussian bell shape via:

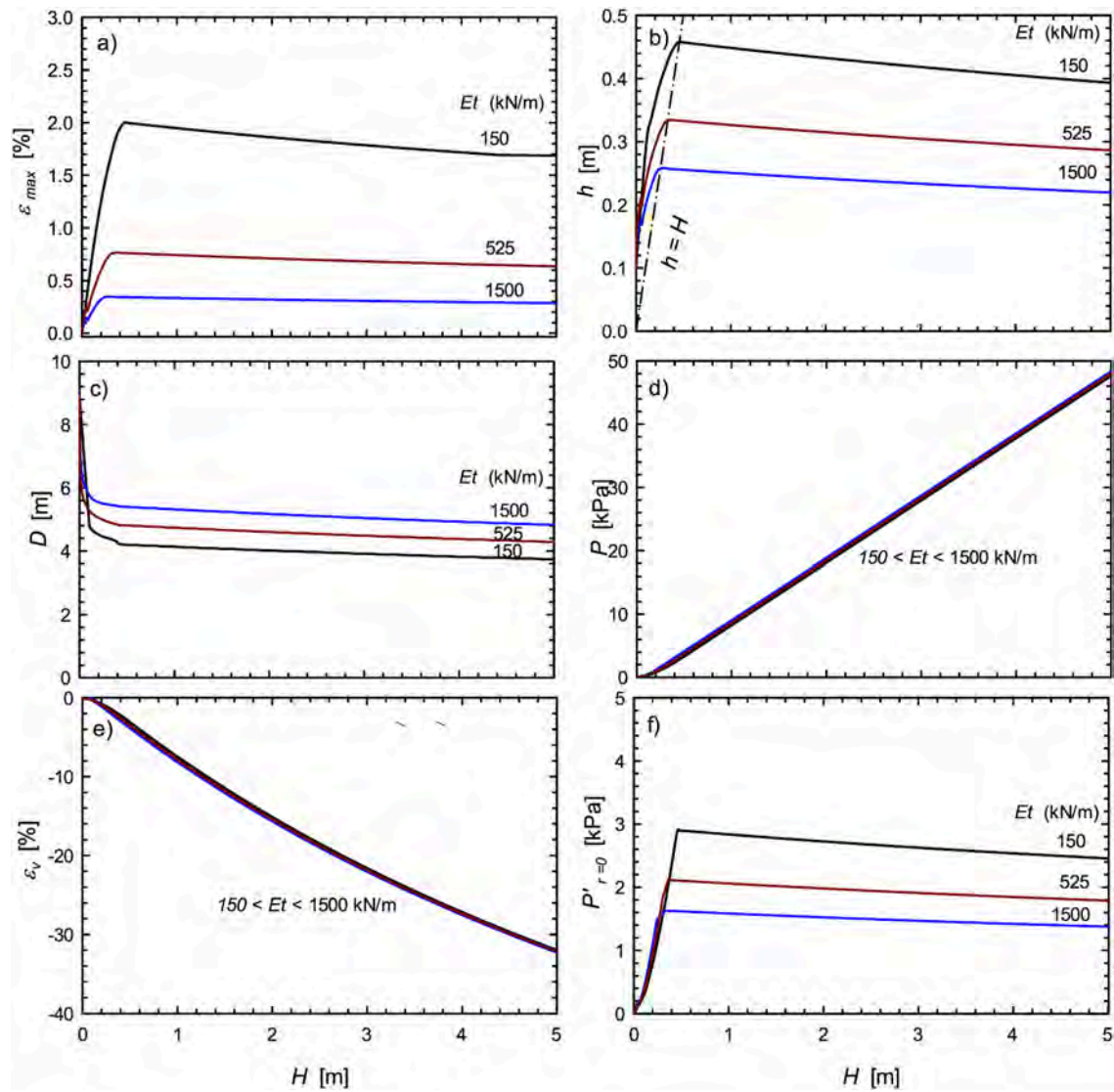$$v \approx 2 \pi h \lambda^2 \tag{2}$$

Fig. 7. Parametric study of bubble parameters to geomembrane stiffness, interface friction, and fluid depth for a small volume of entrapped air. a) Maximum strain, b) bubble height, c) bubble diameter, d) internal pressure, e) volume strain, and f) net pressure at bubble centre. (v_o = 3 m³, S = 10 m).
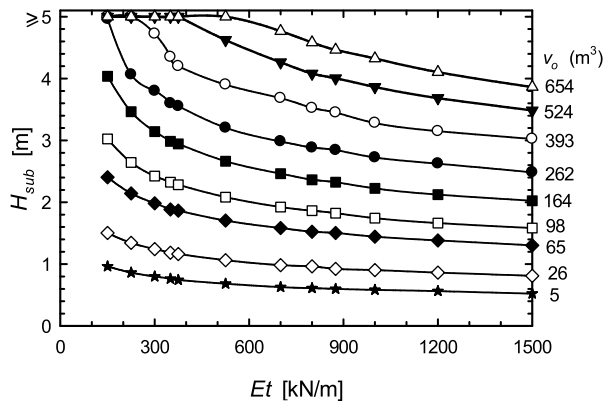

Fig. 8. Fluid depth for bubble submergence. ($\delta = 0$).

where: λ is a dimensionless parameter approximately equal to 0.21 to 0.23 times D for the Gaussian shaped bubble. Since initial volume is the input parameter required to obtained strain, the corresponding theoretical 'initial' bubble volume, v_o, can be obtained from the v vs. H plots like Fig. 10a, b and c for E_t = 375 kN/m. Similar plots for the entire range of stiffnesses considered (150–1500 kN/m) are available as Supplemental Material (Fig. A2). Knowing now v_o and H, geomembrane strain can be obtained from the plots like Fig. 10d, e, and f.

Once a bubble is developed in a geomembrane liner, in addition to strain, the net air pressure in the bubble may also be of interest as it could influence design or operational measures for mitigation. For example, Thiel (2016b) describes measures for using pond bottom slope, venting strips, and physical pushing of bubbles to the pond perimeter where they can be vented through crest vents, all of which are affected by the bubble pressure. Plots of air pressure P vs. H were also tabulated and are available as part of the Supplemental Material (Fig. A3).

5.2. Example 1: Evaluation of an existing bubble

If a water pond lined with an HDPE geomembrane for which values of t = 1.5 mm and E = 250 MPa have been deemed as appropriate, giving
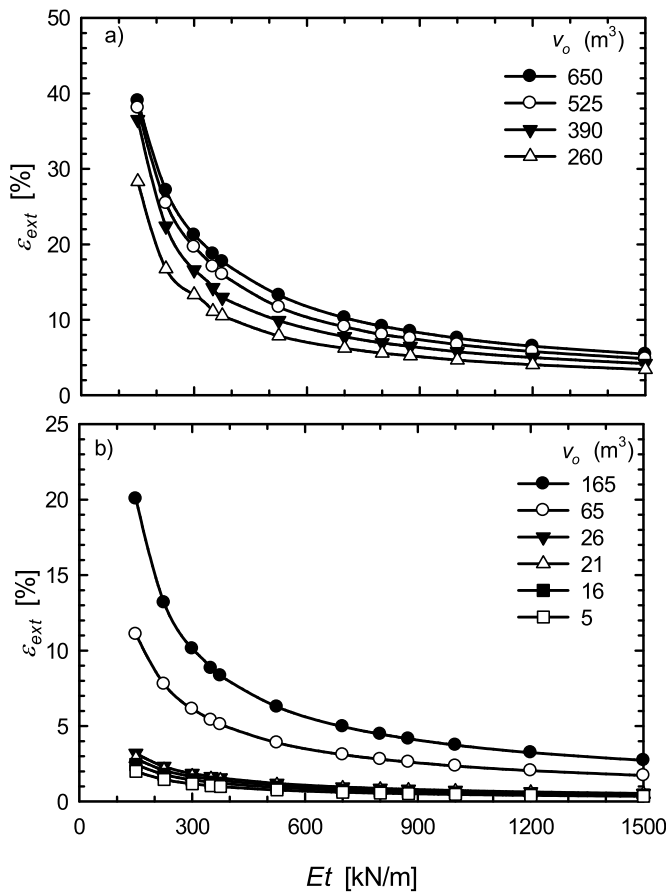
Fig. 9. Overall greatest value of strain developed during pond filling. Value attained at point of submergence for submerged bubbles. (H ≤ 5 m, $\delta = 0$).

$Et = 375$ kN/m, is observed to exhibit an air bubble with a diameter $D = 23.1$ m and height $h = 3.2$ m, in $H = 0.6$ m deep water, the maximum strain ε_{max} in the bubble can be assessed using the design aid charts in three steps. First, using Eq. (2) and taking $\lambda = 0.22$, the bubble volume v can be calculated to be 519 m³. Second, the initial air volume can be estimated by plotting a point on Fig. 10a ($Et = 375$ kN/m) for $H = 0.6$ m for $v = 519$ m³ which yields $v_o \approx 525$ m³. (Note that interpolation can be used for intermediate values of v_o.) Last using Fig. 10d, a maximum strain ε_{max} of 3% is read from the graph using the curve for $v_o = 525$ m³ and $H = 0.6$ m. Similarly, air pressure can be obtained from Fig. A3 in the supplemental materials for $Et = 375$ kN/m to be < 2 kPa.

5.3. Example 2: Developing an operation chart for a particular geomembrane

Once air has been entrapped under the pond liner before filling, or a gas bubble has developed in the liner after filling, it is important to assess the safe water height to which the pond can be operated under without exceeding the geomembrane allowable strain. The design aid charts can be used to develop an operation chart for any geomembrane with known stiffness Et and allowable strain to help determine such water height. The steps to develop an operation chart for a geomembrane with Et of 375 kN/m and allowable strain of 4% are:

1. Using the ε_{max} vs. H charts (Fig. 10d, e, and f for $Et = 375$ kN/m) and for each value of v_o, the water heights that gives a strain of 4% are identified and tabulated in Table 2.
2. Next, using the same ε_{max} vs. H charts, the water heights and corresponding strains to reach complete bubble submersion are obtained for each value of v_o. Complete submersion occurs at the water

height where the overall maximum strain is attained, denoted as H_{sub} and ε_{ext}, respectively. These points are plotted as H_{sub} vs. ε_{ext} in Fig. 11a and H_{sub} vs. v_o in Fig. 11b.
3. From the relationships in Fig. 11, it can be interpolated that when strain is equal to 4%, $H_{sub} = 1.4$ m and $v_o = 42$ m³. This means that for $v_o \leq 42$ m³, the bubble will be completely submerged before reaching the allowable strain and can experience fluid depths greater than 1.4 m without reaching 4% strain. This value is included in Table 2.
4. Last, since all parameters at this point are referenced to v_o, the relationship to current bubble volume is obtained from the v vs. H charts (Fig. 10a, b, and c) as summarized in the last column of Table 2.

The resulting operation chart in Fig. 12 is the graphical form of the data assembled in Table 2. The chart shows the relationship between the water height versus either initial entrapped air volume v_o, Fig. 12a, or current bubble volume v, Fig. 12b, that would result in a geomembrane strain of 4%. This line divides the graph into zones where strain would be less than 4% and where strain would exceed 4%, which would provide a quick check of the pond status before filling, or an existing bubble status after filling.

Before filling, the status of the pond can be checked by estimating the initial bubble volume, or entrapped air volume, from wrinkle size, tributary area, and the operating water height. In this example, a pond with an initial entrapped air less than 42 m³ can be filled safely to any fluid depth, Fig. 12a. Also in this example, it will be unacceptable (in terms of exceeding the geomembrane strain limit) to operate the pond with initial entrapped air v_o of 100 m³ under a water height greater than 1 m, Fig. 12a.

After a bubble develops, the bubble can be checked quickly by the pond operator by determining the current bubble volume and water height and plotting them on the operation chart, Fig. 12b. For example, for the 519 m³ bubble from Example 1 to acceptable, it can be plotted on the operation chart, Fig. 12b, which indicates that the water height can only be increased to 0.85 m before the strain in the bubble exceeds the here in this example the allowable limit of 4% strain.

5.4. Strain directly from deformed shape

In the proposed method, strain can be obtained from measured bubble height and diameter without any simplifying assumptions of strain distribution or displacement trajectory.

The extent to which strain can be calculated solely from the deformed shape of the bubble measured in the field (e.g., using simple to more elaborate surveying techniques) is examined. Any such calculation would require an assumption of deformation trajectory for each point. The prominence of radial displacement to geomembrane bubble strains – and corollary, the error introduced if strain is calculated based only on vertical displacement, can be examined by calculating strain just from the deformed bubble shape and by assuming that any point on the geomembrane surface reached its deformed position by deflecting only in the vertical direction (i.e. zero radial displacement). As noted by Eldesouky and Brachman (2018), this approach has been used when calculating local geomembrane strain from gravel indentations. The deformed surface is divided into segments, separated by distance Δr in the radial direction. The difference in vertical elevation along the segment is Δz. The elongation strain of segment i assuming only vertical displacement, ε_i, is then equal to:

$$\varepsilon_i = \frac{\sqrt{\Delta r_i^2 + \Delta z_i^2} - \Delta r_i}{\Delta r_i} \tag{3}$$

Calculations of strain assuming zero radial displacements at $r = 0$ and the overall maximum value of from all of the segments are compared with the three-dimensional finite-element analysis in Table 3.
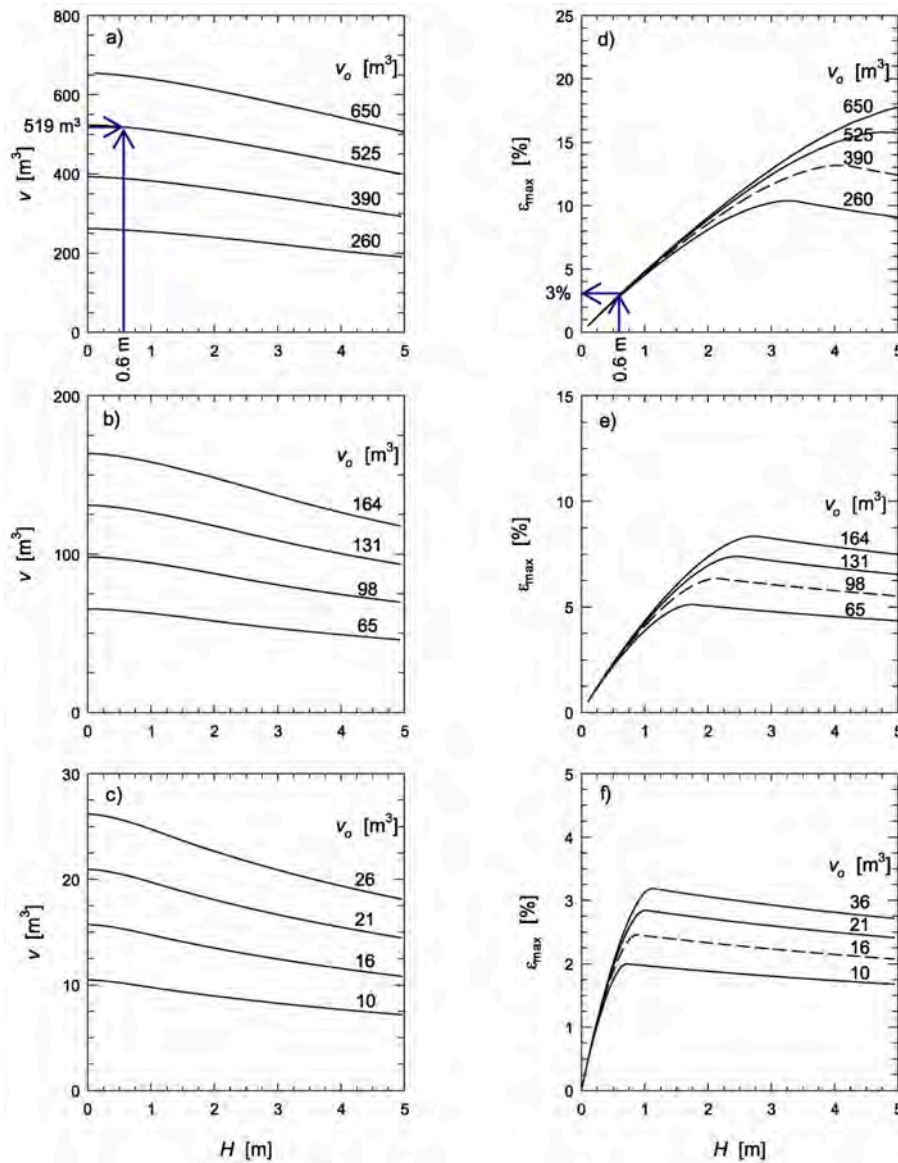
Fig. 10. Charts to obtain: a, b and c) initial volume from existing volume and fluid depth, and d, e and f) maximum strain from initial volume and fluid depth. (Et = 375 kN/m, $\delta = 20°$).

Table 2
Allowable water height for geomembrane with $Et = 375$ kN/m and $\varepsilon = 4\%$.

Initial bubble volume v_o [m³]	Fluid depth to develop $\varepsilon = 4\%$[a] H_{all} [m]	Bubble volume v at H_{all}[b] [m³]
650	0.82	620
525	0.84	514
390	0.86	380
260	0.88	255
164	0.92	159
131	0.94	127
98	0.98	95
65	1.06	62
42[c]	1.40	38
≤26[d]	Submerged	-

[a] Using Fig. 10d, e, and f.
[b] Using Fig. 10a, b, and c.
[c] Interpolated from Fig. 11.
[d] Bubble is submerged before reaching $\varepsilon = 4\%$.

As demonstrated by Eldesouky and Brachman (2018) for gravel indentations, neglecting radial displacements here for the bubble shapes in Fig. 2 significantly underestimates the strain at the bubble centre by calculating very little (<0.7%) to no strain. The error increases as bubble stiffness decreases and fluid depth increases.

The overall maximum strain calculated assuming zero radial displacements is actually greater than the value from the finite-element analysis. For H ≤ 3 m, strains are overestimated by around 10 fold for the low geomembrane stiffness and 5 fold for the high stiffness case, which is most likely overly conservative and may lead to remedial action when it is not necessarily needed. For example, one may deem the strains to be acceptable for the $Et = 1500$ kN/m, $H = 2$ m case based on the finite-element analysis, while the value in excess of 15% strain calculated assuming zero radial displacement would probably warrant action for most geomembrane materials. Using Eq. (3) simply provided unreliable results for the lowest stiffness, deepest pond case considered. The results from the finite-element analysis are therefore recommended for assessing strain in geomembrane bubbles.
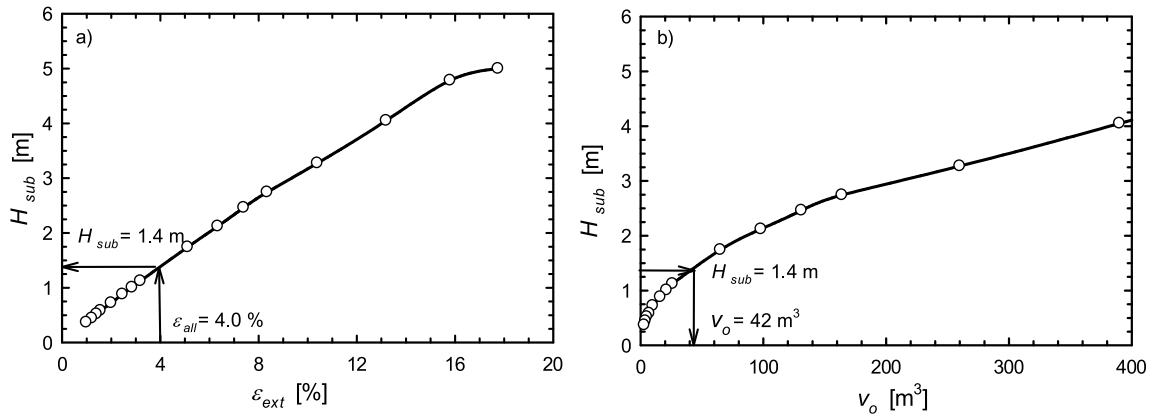
Fig. 11. a) Fluid depth and strain at bubble submergence. b) Fluid depth at submergence vs. initial volume of entrapped air. (Et = 375 kN/m, $\delta = 20°$).
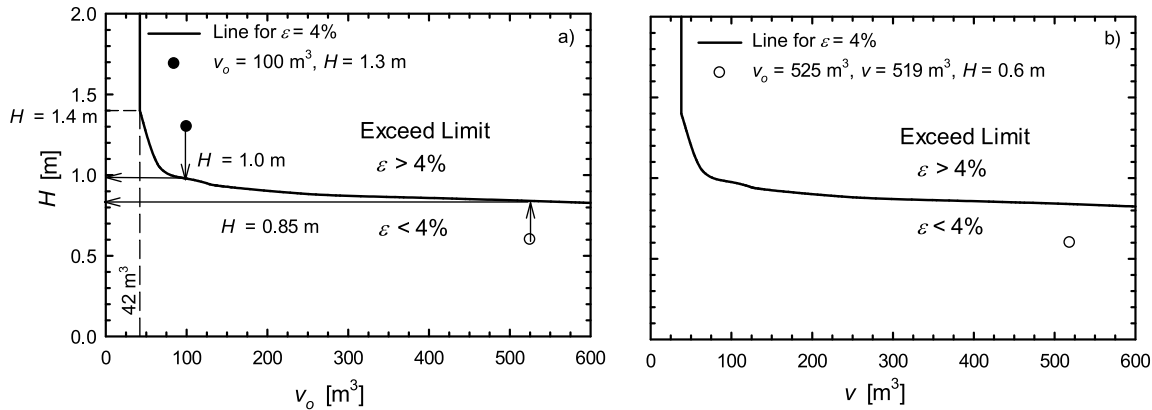

Fig. 12. Operation charts giving fluid depth that would result in a geomembrane strain of 4% as a function of: a) initial entrapped air volume v_o, or b) current bubble volume v. (Et = 375 kN/m, $\delta = 20°$).

Table 3
Comparison of strain (%) from three-dimensional finite-element analysis (3D FEA) with analysis of deformed shape assuming zero radial displacement ($u_r = 0$).

Quantity	Et	H	Method	
	[kN/m]	[m]	3D FEA	Assuming $u_r = 0$
Strain at $r = 0$	150	1	5	0
		2	10	0
		3	17	0
		5	39	<0.1
	1500	1	1	<0.1
		2	3	0.2
		3	4	0.4
		5	5	0.7
Maximum strain	150	1	7	60
		2	15	150
		3	23	300
		5	39	>>300
	1500	1	2	10
		2	4	17
		3	5	20
		5	5	19

5.5. Discussion on allowable strain

This work focusses on the strain demand developed in the geomembrane. Although beyond the scope of this work, the geomembrane resistance in terms of an allowable strain is also important. The allowable strain may be expected to depend on the type of geomembrane, temperature, the presence of any stress/strain concentrations such as welds or scratches (e.g., Gao et al., 2022), the duration of the high stress bubble situation, amplitude and frequency of cyclic stress (such as caused by wind and waves), and any environmental or physical ageing and degradation of the geomembrane (e.g., Rowe and Ewais, 2015). Although allowable strains have been suggested for some materials (e.g., Giroud et al., 1993; Peggs et al., 2005; Koerner, 2005), the selection of an appropriate allowable value for geomembrane bubbles is context-specific and requires considerable engineering judgement. More research on this subject is needed.

6. Conclusions

Geomembrane strains that develop from gas-filled bubbles beneath pond liners were numerically modelled using three-dimensional, geometrically-nonlinear, finite-element analysis. The geomembrane

was simulated as a linear elastic material entrapping an initial volume of gas above a gas impermeable subgrade. Geomembrane deformations and strains were calculated as fluid depth in the pond increased. For the range of geomembrane stiffness, fluid depth, and volume of entrapped gas considered, the following can be concluded:

1) Large bubbles developed greater strains than small bubbles; stiffer geomembranes resulted in shorter bubbles with significantly smaller strains than more flexible ones.
2) Bubble height, maximum strain, and gas pressure all increased as fluid depth increased to the point of bubble submergence, while the bubble diameter and volume decreased.
3) Increasing fluid depth beyond submergence produced incremental decreases in height, diameter, volume and strain, while the gas pressure beneath the bubble increased.
4) The fluid depth at submergence increased with a greater volume of entrapped gas or a decrease in geomembrane stiffness.
5) Bubbles with entrapped air volumes less than an identified critical initial volume can be filled with any water height safely. Reducing the entrapped air volume with design and operational techniques is key to managing and, or mitigating bubbles.
6) Calculating strain solely from the deformed shape and assuming zero radial displacement is most likely overly conservative (over predicting strain by a factor between 5 and 10 relative to the finite-element analysis), and demonstrates the need to consider both vertical and radial displacements as captured by the finite-element analysis.

Strain in existing bubbles can be practically obtained from charts developed from the analysis, like those for one particular value of geomembrane stiffness in Fig. 10 or those for the complete range of stiffnesses examined in the Supplemental Material. Also, operation charts for any geomembrane liner can be developed using the charts and can be a useful tool in pond operation or assessment.

Declaration of competing interest

The authors declare that they have no known competing financial interests or personal relationships that could have appeared to influence the work reported in this paper.

Data availability

Data will be made available on request.

Acknowledgement

Appendix A. Supplementary data

Supplementary data to this article can be found online at https://doi. org/10.1016/j.geotexmem.2023.07.002.

References

ABAQUS, 2017. Abaqus/CAE User Manual 2017. Dassault Systèmes, Providence, RI, USA.

Chappel, M.J., Brachman, R.W.I., Take, W.A., Rowe, R.K., 2012. Large-scale quantification of wrinkles in a smooth black HDPE geomembrane. J. Geotech. Geoenviron. Eng. 138 (8), 671–679. https://doi.org/10.1061/(ASCE)GT.1943-5606.0000643.

Eldesouky, H.M.G., Brachman, R.W.I., 2018. Calculating local geomembrane strains from a single gravel particle with thin plate theory. Geotext. Geomembranes 46 (1), 101–110. https://doi.org/10.1016/j.geotexmem.2017.10.007.

Eldesouky, H.M.G., Brachman, R.W.I., 2020. Viscoplastic modelling of HDPE geomembrane local stresses and strains. Geotext. Geomembranes 48 (1), 41–51. https://doi.org/10.1016/j.geotexmem.2019.103503.

Eldesouky, H.M.G., Brachman, R.W.I., 2023. Calculating local geomembrane strains from gravel particle indentations with thin plate theory. Geotext. Geomembranes 51 (1), 56–72. https://doi.org/10.1016/j.geotexmem.2022.09.007.

Fan, J., Rowe, R.K., 2022. Effect of subgrade on tensile strains in a geomembrane for tailings storage applications. Can. Geotech. J. 60 (1), 18–30. https://doi.org/10.1139/cgj-2022-0019.

Gao, W., Kavazanjian Jr., E., Wu, X., 2022. Numerical study of strain development in high-density polyethylene geomembrane liner system in landfills using a new constitutive model for municipal solid waste. Geotext. Geomembranes 50 (2), 216–230. https://doi.org/10.1016/j.geotexmem.2021.09.007.

Gassner, F., 2017. Development and management of geomembrane liner hippos. Geotext. Geomembranes 45 (6), 702–706. https://doi.org/10.1016/j.geotexmem.2017.08.007.

Giroud, J.P., Goldstein, J.S., 1982. Geomembrane liner design. Waste Age 13, 27–30.

Giroud, J.P., Soderman, K., Monroe, M., 1993. Mechanical design of geomembrane applications. In: Geo '93. Vancouver, Canada, pp. 1455–1468.

Guo, W., Chu, J., Zhou, B., Sun, L., 2016. Analysis of geomembrane whale due to liquid flow through composite liner. Geotext. Geomembranes 44 (3), 247–253. https://doi:10.1016/j.geotexmem.2015.11.003.

Koerner, R.M., 2005. In: Designing with Geosynthetics, fifth ed. Pearson Education, Inc., New Jersey.

Lavoie, F.L., Valentin, C.A., Kobelnik, M., Lins da Silva, J., Lopes, M.D.L., 2020. HDPE geomembranes for environmental protection: two case studies. Sustainability 12 (20), 8682.

Lavoie, F.L., Kobelnik, M., Valentin, C.A., Tirelli, É.F.D.S., Lopes, M.D.L., Silva, J.L.D., 2021. Laboratory study of the ultraviolet radiation effect on an HDPE geomembrane. Membranes 11 (6), 390.

Lavoie, F.L., Kobelnik, M., Valentin, C.A., Tirelli, É.F.D.S., Lopes, M.D.L., Silva, J.L.D., 2022. Evaluation of exhumed HDPE geomembranes used as a liner in Brazilian shrimp farming ponds. Case Stud. Constr. Mater. 16, e00809 https://doi.org/10.1016/j.cscm.2021.e00809.

Marcotte, B.A., Fleming, I.R., 2021. Direct measurement of geomembrane strain from aggregate indentations. Geosynth. Int. 28 (5), 464–478.

Marcotte, B.A., Fleming, I.R., 2022. Design guidance for protection of geomembrane liners in landfill applications. Can. Geotech. J. 59 (5), 743–757. https://doi.org/10.1139/cgj-2021-0222.

Marta, A., Armstrong, C., 2020. Brittle stress cracking of HDPE geomembrane caused by localized over heating of fusion wedge welds and whales. In: Proc. GeoAmericas 2020 – 4th Pan-American Conference on Geosynthetics (Rio de Janeiro, Brazil).

Nower, M., Elashaal, A., El-serafy, S., 2020. Factors affecting the performance of geomembrane as an enhancement measure for seepage control in solar pond. Int. J. Sci. Eng. Res. 11 (12), 1168–1171.

Peggs, I.D., 2012. Impact of variable stresses on accelerated stress cracking of HDPE wrinkles. In: Proc. GeoAmericas 2012. 2nd Pan-American Geosynthetics Congress, Lima, Peru.

Peggs, I.D., Schmucker, B., Carey, P., 2005. Assessment of maximum allowable strains in polyethylene and polypropylene geomembranes. In: Proc. Geo-Frontiers. ASCE, Reston, VA.

Rarison, R.F.M., Mbonimpa, M., Bussière, B., 2022. Effects of freeze–thaw cycles on the properties of polyethylene geomembranes. Geosynthetic Int. Published online. https://doi.org/10.1680/jgein.21.00043a. August 31, 2022.

Rentz, A.K., Brachman, R.W.I., Take, W.A., Rowe, R.K., 2017. Comparison of wrinkles in white and black HDPE geomembranes. J. Geotech. Geoenviron. Eng. 143, 04017033 https://doi.org/10.1061/(ASCE)GT.1943-5606.0001715.

Rowe, R.K., Ewais, A.M.R., 2015. Ageing of exposed geomembranes at locations with different climatological conditions. Can. Geotech. J. 52 (3), 326–343.

Rowe, R.K., Chappel, M.J., Brachman, R.W.I., Take, W.A., 2012. Field study of wrinkles in a geomembrane at a composite liner test site. Can. Geotech. J. 49 (10), 1196–1211. https://doi.org/10.1139/t2012-083.

Sharma, S.M., Tian, K., Tanyu, B., 2023. Evaluation of Atactic Polypropylene (APP) geomembranes used as liners for salt ponds. Geotext. Geomembranes 51 (1), 165–178.

Thiel, R., 2016a. Analysis of stresses and strains in geomembrane gas bubbles that occur in surface impoundments. In: Geosynthetics, Forging a Path to Bona Fide Engineering Materials. American Society of Civil Engineers, Reston, VA, pp. 244–255. https://doi.org/10.1061/9780784480182.022.

Thiel, R., 2016b. Recommendations for design of exposed geomembrane-lined ponds to control uplifting gas pressures. Proc. 6th Eur. Geosynth. Conf 25–28.

Thiel, R., Giroud, J.P., 2011. Important considerations for geomembrane-lined ponds. In: Proc. 13th Int. Waste Management and Landfill Symp, p. 12.

Thiel, R., Eldesouky, H., Brachman, R.W.I., 2022. Traditional vs numerical methods to estimate pressures and strains in pond geomembrane bubbles. Proc. 7th Eur. Geosynth. Conf (in press).

Wallace, R., Giroud, J.P., Shanks, M., 2006. Impacts of construction practices and reservoir filling on geomembrane uplift. In: Proc. 8th Int. Conf. Geosyn, pp. 615–618.

Wang, L., Liu, S., Shen, C., Lu, Y., 2020. Laboratory test and modelling of gas pressure under geomembrane subjected to the rise of groundwater in plain reservoirs. Geotext. Geomembranes 49 (1), 81–96. https://doi.org/10.1016/j.geotexmem.2020.09.006.

Zhang, X.L., Wu, Y.Y., Ma, Z.Y., Yin, C.J., 2023. Mechanical properties of PVC geomembrane based on non-contact measurement. Geosynth. Int. 30 (3), 259–273. https://doi.org/10.1680/jgein.21.00104.

Glossary

D: bubble diameter
E: geomembrane modulus
Et: geomembrane stiffness
H: fluid depth
H_{sub}: fluid depth required for bubble submergence
h, h_o: bubble height, initial bubble height
P, P_w: air pressure, water pressure
P', P'_{ext}: net pressure, extreme net pressure
R: initial radius of geomembrane $= S/2$

r, z: polar coordinates in *r-z* space
S: dimension of pond region contributing to bubble formation
t: geomembrane thickness
u_r: displacement in radial *r* direction
v, v_o: bubble volume, initial bubble volume
δ: interface friction angle between geomembrane and subgrade
ε_r: radial strain in geomembrane
ε_{max}: maximum strain in geomembrane
ε_{ext}: extreme strain in geomembrane during filling process
λ: Gaussian bell shape standard deviation